

Calibration-based two-frequency projected fringe profilometry: a robust, accurate, and single-shot measurement for objects with large depth discontinuities

Wei-Hung Su

*Department of Material Science and Optoelectronic Engineering, National Sun Yat-Sen University
Kaohsiung 804, Taiwan
wxs156@mail.nsysu.edu.tw*

Hongyu Liu

Department of Electrical Engineering, The Pennsylvania State University, University Park, PA 16802

Abstract: An improved method is proposed to perform calibration-based fringe projected profilometry using a two-frequency fringe pattern for the 3D shape measurements of objects with large discontinuous height steps. A fabrication scheme for the two-frequency pattern is described as well. The proposed method offers following major advantages: (1) only one phase measurement needed for operation, (2) easiness for calibration, (3) robust performance, especially for automatic phase unwrapping, and (4) more flexible data acquisition for complex objects. This makes it possible for a single-shot measurement of dynamic objects with discontinuities. Both theoretical descriptions and experimental demonstrations are provided.

©2006 Optical Society of America

OCIS codes: (120.4630) Optical Inspection; (110.6880) Three-dimensional image acquisition.

References and links

1. G. Indebetouw, "Profile measurement using projection of running fringes," *Appl. Opt.* **17**, 2930-2933 (1978).
2. V. Srinivasan, H. C. Liu, and M. Halioua, "Automated phase-measuring profilometry of 3-D diffuse objects," *Appl. Opt.* **23**, 3105-3108 (1984).
3. M. Takeda and K. Motoh, "Fourier transform profilometry for the automatic measurement of 3-D object shaped," *Appl. Opt.* **22**, 3977-3982 (1983).
4. X. Su, and W. Chen, "Fourier transform profilometry: a review," *Opt. Lasers Eng.* **35**, 263-284 (2001).
5. K. G. Larkin and B. F. Oreb, "Design and assessment of symmetrical phase-shifting algorithms," *J. Opt. Soc. Am. A* **9**, 1740-1748 (1992).
6. V. Y. Su, G von Bally, and D. Vukicevic, "Phase-stepping grating profilometry: utilization of intensity modulation analysis in complex objects evaluation," *Opt. Commun.* **98**, 141-150 (1993).
7. Y. Surrel, "Design of algorithms for phase measurements by the use of phase stepping," *Appl. Opt.* **35**, 51-60 (1996).
8. F. Chen, G. M. Brown, and M. Song, "Overview of three-dimensional shape measurement using optical methods," *Opt. Eng.* **39**, 10-22 (2000).
9. W. H. Su, H. Liu, K. Reichard, S. Yin, and F. T. S. Yu, "Fabrication of digital sinusoidal gratings and precisely controlled diffusive flats and their application to highly accurate projected fringe profilometry," *Opt. Eng.* **42**, 1730-1740 (2003).
10. D. C. Ghiglia and L. A. Romero, "Robust two-dimensional weighted and unweighted phase unwrapping that uses fast transforms and iterative methods," *J. Opt. Soc. Am. A* **11**, 107- (1994).
11. K. A. Stetson, J. Wahid, and P. Gauthier, "Noise-immune phase unwrapping by use of calculated wrap regions," *Appl. Opt.* **36**, 4830-4838 (1997).
12. A. Collaro, G. Franceschetti, F. Palmieri, and M. S. Ferreiro, "Phase unwrapping by means of genetic algorithms," *J. Opt. Soc. Am. A* **15**, 407-418 (1998).
13. J.-J. Chyou, S.-J. Chen, and Y.-K. Chen, "Two-dimensional phase unwrapping with a multichannel least-mean-square algorithm," *Appl. Opt.* **43**, 5655-5661 (2004).

14. J. M. Huntley and H. O. Saldner, "Temporal phase-unwrapping algorithm for automated interferogram analysis," *Appl. Opt.* **32**, 3047-3052 (1993).
 15. H. O. Saldner and J. M. Huntley, "Profilometry using temporal phase unwrapping and a spatial light modulator-based fringe projector," *Opt. Eng.* **36**, 610-615 (1997).
 16. K. Creath, "Step height measurement using two-wavelength phase-shifting interferometry," *Appl. Opt.* **26**, 2810-2816 (1987).
 17. H. Zhao, W. Chen, and Y. Tan, "Phase-unwrapping algorithm for the measurement of three-dimensional object shapes," *Appl. Opt.* **33**, 4497-4500 (1994).
 18. D. R. Burton and M. J. Lalor, "Multichannel Fourier fringe analysis as an aid to automatic phase unwrapping," *Appl. Opt.* **33**, 2939-2948 (1994).
 19. Y. Hao, Y. Zhao, and D. Li, "Multifrequency grating projection profilometry based on the nonlinear excess fraction method," *Appl. Opt.* **38**, 4106-4110 (1999).
 20. E. B. Li, X. Peng, J. Xi, J. F. Chicharo, J. Q. Yao, and D.W. Zhang, "Multi-frequency and multiple phase-shift sinusoidal fringe projection for 3D profilometry," *Opt. Express* **13**, 1561-1569 (2005).
 21. M. Takeda, Q. Gu, M. Kinoshita, H. Takai, and Y. Takahashi, "Frequency-multiplex Fourier-transform profilometry: a single-shot three-dimensional shape measurement of objects with large height discontinuities and/or surface isolations," *Appl. Opt.* **36**, 5347-5354 (1997).
 22. J. L. Li, H. J. Su, and X. Y. Su, "Two-frequency grating used in phase-measuring profilometry," *Appl. Opt.* **36**, 277-280 (1997).
 23. H. Liu, W. H. Su, K. R., and S. Yin, "Calibration-based phase-shifting projected fringe profilometry for accurate absolute 3D surface profile measurement," *Opt. Commun.* **216**, 65-80 (2003).
 24. L. B. Jackson, *Digital Filters and Signal Processing* (Toppan, 1996), Chap. 6.
-

1. Introduction

Projected fringe profilometry has been one of the most popular non-scanning methods for the 3D surface profile inspection [1, 2]. It uses a fringe pattern projected to the inspected object and then evaluates the phase of the fringe obtained from a different viewpoint to retrieve the depth information. With proper phase-extraction schemes, such as Fourier transform method [3,4], and phase shifting method [5-7], depth accuracy better than one part in ten thousandth of the field of view can be achieved [8-9].

One of the current trends in the development of 3D inspection is the accurate measurement of complex objects. However, it is a challenge to analyze surfaces with lots of discontinuities. Phase unwrapping [10-13], the inevitable procedure to remove the phase jumps in order to recover the absolute phase, will encounter ambiguity to distinguish the local fringe order.

Several projection methods have been developed to overcome the discontinuities. They can be roughly divided into two categories, namely temporal projection algorithms and spatial projection algorithms. In the temporal projection algorithms, for example, Saldner and Huntley [14, 15] project a number of fringe patterns with slightly different frequencies to the isolated surfaces in sequence of time. The phase at each pixel is measured as a function of time. Unwrapping is then performed along the time axis. An alternative modification is the use of multi-frequency interferometer [16-20]. Two or more gratings with slightly different frequencies are temporally projected onto the inspected object. Unwrapping is retrieved from the comparison of each phase map.

In the method of spatial projection algorithms, M. Takeda et al. [21] has presented a method based on spatial frequency multiplexing combined with the Gushow-Solodkin phase unwrapping algorithm. With Fourier transform method it requires only one measurement frame to inspect discontinuous surfaces. Jie-Lin Li et al. [22] propose a phase-shifting scheme of a two-frequency pattern in which one frequency is N times as large as the other. The low frequency is more tolerant to physical discontinuities, whereas the higher one can refine the result. Therefore, the high-frequency phases are unwrapped with reference to the low-frequency phases.

In general, temporal projection algorithms provide more accurate information of discontinuities since several frames are measured. However, the longer measurement procedure makes it impractical for inspection of dynamic objects. It seems that spatial projection algorithms are more efficient for the real-time performance. Unfortunately, since

the pattern involves a couple of frequencies, the sampling density and visibility of fringes on the recorded image is relatively low.

To maintain the advantages (i.e., one shot measurement for dynamic objects with large height steps) and eliminate the limitations (low visibility and sampling density), in this paper, we investigate an improvement on the above methods [21, 22] based on Fourier transform method using a two-frequency pattern. To suit the needs of high-accuracy measurements, a digital two-frequency pattern has been designed and fabricated based on the optical lithography technique. The designed pattern can substantially increase the measurement accuracy because it offers (1) high geometrical accuracy ($< 0.5\mu\text{m}$); (2) high contrast ratio; and (3) very low high-order harmonic distortions.

2. Properties of the two-frequency fringe pattern

The two-frequency pattern is the combination of two sets of fringes with different frequencies: one frequency is P ($P=3, 4, 5 \dots$) times larger than the other. Its transmittance is represented as

$$t(x) = \frac{1}{2} + \frac{1}{4} \cos\left(\frac{2\pi}{d} x\right) + \frac{1}{4} \cos\left(\frac{2\pi}{Pd} x\right) \quad (1)$$

The two-frequency pattern is designed and fabricated based on the lithography technique. This designed pattern with two sets of fringes is a quantized version of its continuous counterpart - it is discrete in both space and transmittance. The quantization scheme divides one period of the higher-frequency sinusoid into N intervals. Shown in Fig. 1 is an example, in which $N = 16$, and $P = 5$.

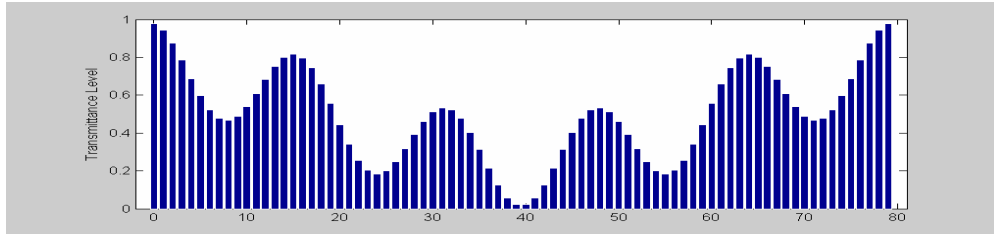


Fig. 1. Quantization scheme used for generating a digital sinusoidal grating from its continuous counterpart.

The averaged transmittance of the n th interval is then computed as,

$$\begin{aligned} \bar{t}(n) &= \frac{1}{w} \int_{nw}^{(n+1)w} [t(x)] dx \\ &= \frac{1}{2} + \frac{1}{4} \text{sinc}\left(\frac{\pi}{N}\right) \cos\left(\frac{2n+1}{N} \pi\right) + \frac{1}{4} \text{sinc}\left(\frac{\pi}{PN}\right) \cos\left(\frac{2n+1}{PN} \pi\right) \end{aligned} \quad (2)$$

where $w \equiv d/N$ is the width of the intervals, and $\text{sinc}(x) \equiv \frac{\sin(x)}{x}$.

The transmittance ranging from zero to full transmission is quantized into M levels as well. Its quantized transmittance t_n for the n th interval can be found as

$$t_n = \frac{[M \bar{t}(n)]}{M}, \quad (3)$$

where $[]$ denotes rounding to the nearest integer.

To represent different quantized transmittance levels, an area-encoding scheme is adopted. In this scheme, M cells are used as a group to represent a quantized transmittance level t_n . Different transmittance levels are implemented by setting the total number of transparent cells to the represented level. The patterns resulted from such an encoding method for several transmittance levels are outlined as Fig. 2.

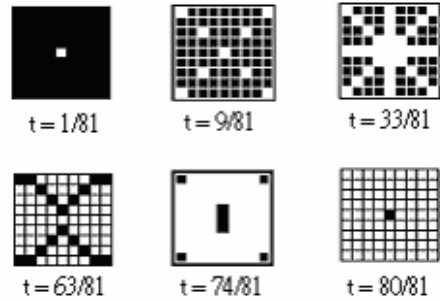


Fig. 2. Patterns resulted from an area-encoding scheme for representing discrete transmittance levels.

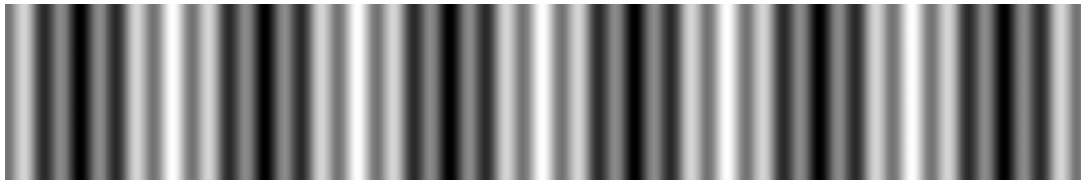


Fig. 3. Appearance of a designed digital two-frequency pattern.

An example of the pattern which contains two sets of fringes with different frequencies resulted from the above design procedure is shown in Fig. 3. In this pattern, the period of the low frequency and the high frequency are $960\mu\text{m}$ and $192\mu\text{m}$, respectively. The period of the higher-frequency sinusoid is divided into 16 intervals along the normal direction of the fringe lines. Its transmittance ranging from zero to full transmission is quantized into 100 levels. Figure 4 shows the spectrum of this digital two-frequency pattern. There is no noticeable high-order harmonics. The spectrum illustrates that of the digital pattern is fabricated with high controlled contrast ratio, and very low harmonic distortion (third-order harmonic is less than 0.5% after low-pass filtering by the imaging system). Thus, it allows excellent performance even when the grating is used under a magnification factor that is slightly different from the designated one or certain degree of misalignment between a CCD pixel and the image of the grating.

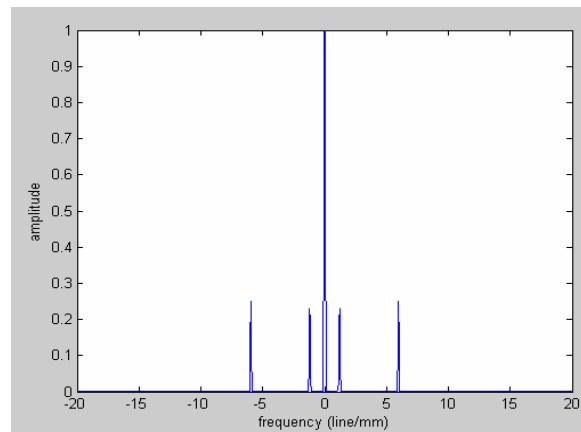


Fig. 4. Fourier spectrum of the image of a digital two-frequency pattern.

3. Phase-extraction for two-frequency patterns

To illustrate the basic concept of this technique, consider the designed two-frequency pattern projected onto a tested surface. The intensity distribution with distorted fringes obtained by the CCD sensor array can be represented as

$$I(x, y) = a(x, y) + h(x, y) \cos \varphi_h(x, y) + l(x, y) \cos \varphi_l(x, y), \quad (4)$$

where φ_h and φ_l are phases of the high frequency and the low frequency, respectively. They can be expressed more specifically as

$$\begin{cases} \varphi_h(x, y) = \frac{2\pi}{d}x + \Delta\varphi(x, y), \\ \varphi_l(x, y) = \frac{2\pi}{Pd}x + \frac{\Delta\varphi(x, y)}{P} \end{cases} \quad (5)$$

where $\Delta\varphi$ is the distorted phase caused by depth variation.

Representing the cosine function in Eq. (4) as a sum of complex exponential functions, one can have

$$\begin{aligned} I(x, y) = & a(x, y) + \tilde{h}(x, y) \exp\left(j \frac{2\pi}{d}x\right) + \tilde{h}^*(x, y) \exp\left(-j \frac{2\pi}{d}x\right) \\ & + \tilde{l}(x, y) \exp\left(j \frac{2\pi}{Pd}x\right) + \tilde{l}^*(x, y) \exp\left(-j \frac{2\pi}{Pd}x\right), \end{aligned} \quad (6)$$

where $j = \sqrt{-1}$, and “*” represents a complex conjugate. Complex modulation $\tilde{h}(x, y)$ and $\tilde{l}(x, y)$ are of the following form,

$$\tilde{h}(x, y) = \frac{1}{2} h(x, y) \exp[j\Delta\varphi(x, y)], \quad (7a)$$

$$\tilde{l}(x, y) = \frac{1}{2} l(x, y) \exp\left[\frac{j\Delta\varphi(x, y)}{P}\right]. \quad (7b)$$

The one-dimensional Fourier transform of Eq. (6) gives

$$\begin{aligned} F(f_x, y) = & A(f_x, y) + \tilde{H}(f_x - 1/d, y) + \tilde{H}^*(f_x + 1/d, y) \\ & + \tilde{L}(f_x - 1/Pd, y) + \tilde{L}^*(f_x + 1/Pd, y), \end{aligned} \quad (8)$$

where $A(f_x, y)$, $\tilde{H}(f_x, y)$ and $\tilde{L}(f_x, y)$ are complex Fourier amplitudes. The terms $\tilde{H}(f_x - 1/d, y)$ and $\tilde{L}(f_x - 1/Pd, y)$ can be picked up by performing bandpass filtering. By applying the inverse Fourier transform to $\tilde{H}(f_x - 1/d, y)$ and $\tilde{L}(f_x - 1/Pd, y)$, the following complex signal can be recovered,

$$s_h(x, y) = h(x, y) \exp\left(j \frac{2\pi}{d}x\right) \exp[j\Delta\varphi(x, y)], \quad (9a)$$

$$s_l(x, y) = l(x, y) \exp\left(j \frac{2\pi}{Pd}x\right) \exp\left[\frac{j\Delta\varphi(x, y)}{P}\right]. \quad (9b)$$

The desired phase distribution of the higher frequency from Eq. (9a) is then given by

$$\Phi_h(x, y) = \tan^{-1} \left\{ \frac{\text{Im}[s_h(x, y)]}{\text{Re}[s_h(x, y)]} \right\}, \quad (10a)$$

and the phase distribution of the lower one according to Eq. (9b) is

$$\Phi_l(x, y) = \tan^{-1} \left\{ \frac{\text{Im}[s_l(x, y)]}{\text{Re}[s_l(x, y)]} \right\}. \quad (10b)$$

Note that Φ_h and Φ_l are within the interval between $-\pi$ and π , and need to be unwrapped to obtain the absolute phases φ_h and φ_l . In the above phase calculation, the unwanted DC term $a(x,y)$ is eliminated during the filtering process and the multiplicative noise is cancelled out by the division operation in Eq. (10a) and (10b).

In order to use this method, the spectra of the modulated signal and the DC term must be suitably separated in the frequency domain. This can be easily achieved in the calibration by choosing a proper grating period.

4. Phase unwrapping

The procedure of phase unwrapping is performed both to the high frequency phase Φ_h and the low frequency phase Φ_l . It is reasonable to assume that the frequency of the lower one is low enough that no discontinuity is larger than its equivalent wavelength. Thus, errors of phase unwrapping for the high frequency pattern can be corrected from the absolute phase map of the lower frequency one.

A parameter Q which plays an important role in determining the ambiguity condition is defined as

$$Q = \left[\frac{\text{Unwrap}\{\Phi_h\} - P \cdot \text{Unwrap}\{\Phi_l\}}{2\pi} \right], \quad (11)$$

where $\text{Unwrap}\{\}$ denotes the phase-unwrapping operator, and $[]$ denotes rounding to the nearest integer. For measurements of continuous surfaces, Q is equal to zero. Therefore, the unwrapped phase $\text{Unwrap}\{\Phi_h\}$ at the discontinuous area can be automatically carried out if Q is not zero. The unwanted errors can be compensated with this term $\text{Unwrap}\{\Phi_h\} - 2\pi Q$.

5. System calibrations

Figure 5 shows the coordinate systems in a typical non-telecentric projected fringe profile measurement system. A fringe pattern that lies in the $X_g Y_g$ plane with fringes normal to axis X_g is projected to the tested object. World coordinate system XYZ is a fixed reference system for representing the shape of the tested object. The CCD sensor array, which is located in the coordinate system RC , records the distorted fringes on the object via the imaging lens. The origin of the camera coordinate system, UVW , is the nodal point of the imaging lens, while the origin of the projection system, $X_p Y_p Z_p$, is the nodal point of the projection lens. Axis W and Z_p coincides with the optical axis of the imaging lens and projection lens, respectively.

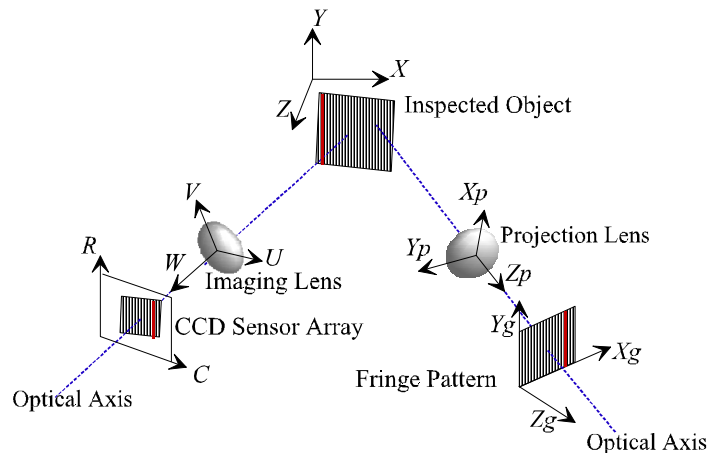


Fig. 5. Coordinate systems in a non-telecentric projected fringe measurement system.

Even perspective errors or distortions from the lens system are involved, our previous work [23] has shown that x and y can be expressed as functions of z , as given by

$$\begin{cases} x = a_1 z + a_o, \\ y = b_1 z + b_o, \end{cases} \quad (12)$$

where a_1 , a_o , b_1 , and b_o can be determined by a set of depth values and corresponding transverse positions. The conversion between the phase and the depth information can be determined by:

$$z = \frac{m'_1 \varphi + m'_0}{n'_1 \varphi + 1} + \sum_{0 \leq i \leq 6} \left[\frac{g_i - h_i \varphi}{n'_1 \varphi + 1} \left(\frac{m'_1 \varphi + m'_0}{n'_1 \varphi + 1} \right)^i \right], \quad (13)$$

where z and φ are the depth position and unwrapped phase, and m'_1 , m'_0 , n'_1 , g_i , and h_i are undetermined coefficients from the optical system. The first part of Eq. (13) can be recognized as the ideal phase-to-depth relation, while the second term originates from distortions. For well-behaved systems, the distorted image points are very close to their ideal counterparts.

The estimation of Eq. (13) can be represented as the polynomial

$$z(\varphi) = \sum_{i=0}^n c_i \varphi^i + \sum_{i=0}^m c_{-i} \varphi^{-i}, \quad (14)$$

where c_i and c_{-i} are coefficients of the polynomial. With a sufficient set of phase values and corresponding depth values, the coefficients can be carried out.

6. Experiments

6.1 3D shape measurements

As an experimental example, a fan blade attached with a wedged object was selected as the testing sample. Large step discontinuities occurred between the fan blade and the wedged object. A monochrome sensor array with 1024×1024 pixels at 12-bit pixel resolution was used to record the distorted fringes. Shown in Fig. 6 is the recorded image in which a two-frequency fringe pattern was projected on this testing object. In this pattern, one frequency was five times larger than the other. The frequency of the lower one was low enough that no discontinuity was larger than its equivalent wavelength.

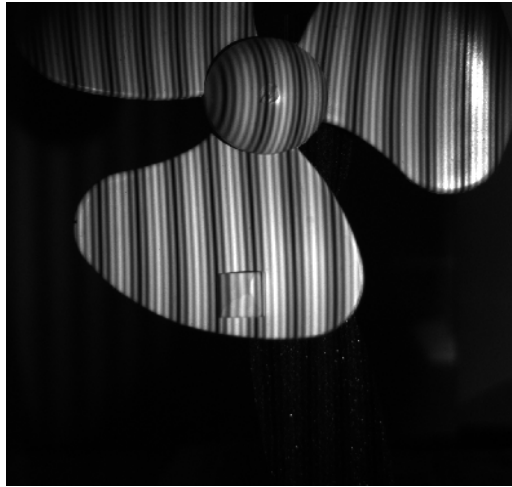


Fig. 6. Appearance of a two-frequency fringe pattern projected to the testing object. A 12-bit camera with 1024×1024 pixels was used to record the fringes.

The low-frequency phase and the high-frequency phase were evaluated by Fourier transform method. Figures 7(a) and 7(b) shows the phase maps of the high frequency and the

low frequency, respectively. Each figure is attached a color bar to identify the correspondence between the phase value and the color.

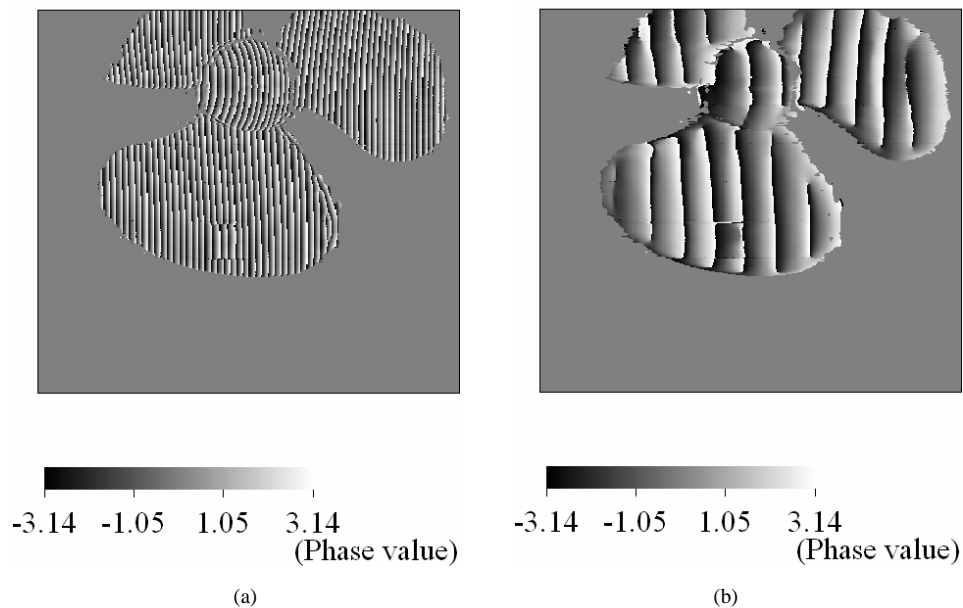


Fig. 7. Phase map of (a) the higher frequency, and (b) the lower frequency. Note that the phases were within the interval between $-\pi$ and π . Phase values close to π were displayed in the bright regions; while areas shown in dark indicated that the phases were close to $-\pi$, as shown in the color bar.

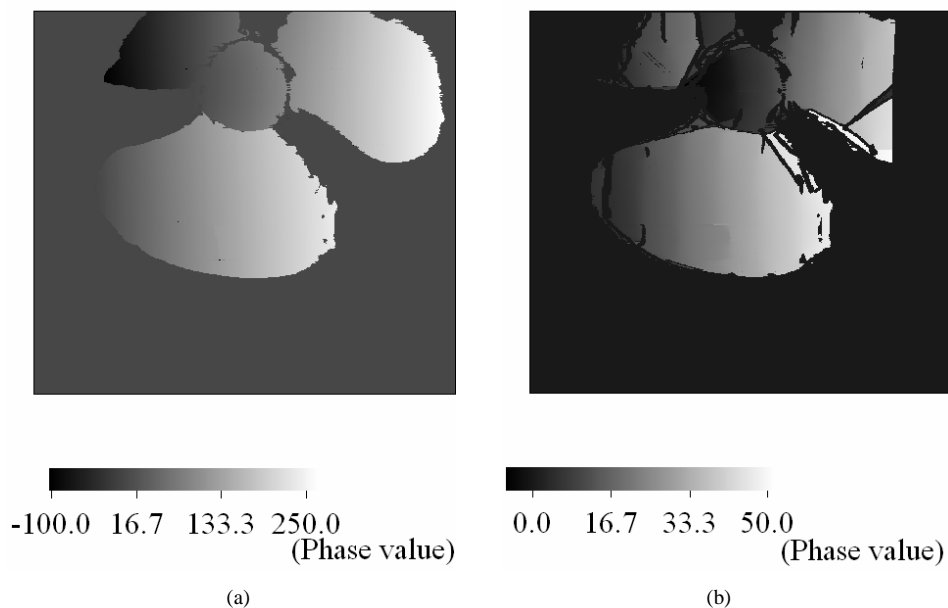


Fig. 8. Unwrapped phase map from Fig. 7. (a) The higher frequency, and (b) the lower frequency. Phases were mapped to the corresponding colors: the brighter one represented the larger phase value.

For the high-frequency pattern, it is difficult to directly distinguish the local fringe order when discontinuity is larger than its equivalent wavelength. Thus, as depicted in Fig. 8(a), the uncorrected phase jumps occurred. With reference to the low-frequency phases, or say, by evaluation of Eq. (11), the uncorrected phase jumps could be identified. Shown in Fig. 8(b) is the unwrapped phase map of the low frequency. The corrected absolute phase map of the high frequency is given in Fig. 9.

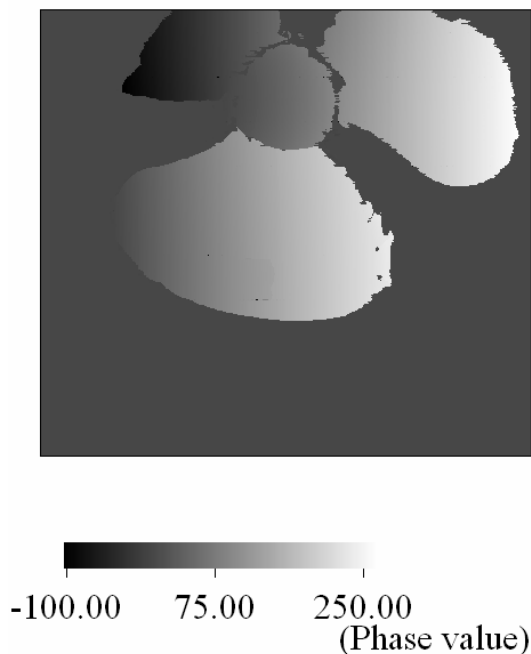


Fig. 9. Unwrapped phase map of the higher frequency. Errors while phase unwrapping have been corrected.

With Eq. (14), depth profile of the detecting sample could be found out from the corrected absolute phase map. Its transverse profile could be computed by Eq. (12). Figure 10 shows the 3D shape of the testing sample reconstructed by our proposed method.

6.2 Error analysis

The sources of errors could be roughly divided into three categories: (1) errors from the calibration scheme, (2) errors from the optical system, and (3) errors from the image processing.

The calibration scheme could produce enormous errors while the coefficients of Eq. (12) and (14) were not accurate. We had proposed a method to design the calibration tools to reduce such kind of errors [9]. Accuracy of the calibration tools could be achieved in the sub-micrometer range. When the order of the polynomial, n , increased, Eq. (14) could become more accurate as well. Our experiments had shown that the coefficients could be carried out in the order of sub-micron accuracy while $n = 5$.

Errors from the optical system were mainly introduced by perspective distortion, projection/imaging quality of the lens system, geometric accuracy of the fringe pattern, and sampling density of the CCD camera. With a high resolution CCD camera and a proposed digital pattern, this kind of errors could be minimized after system calibrations. This makes it possible to achieve micron-range accuracy [9, 23].

In our experiment, errors caused by image processing were mainly from the uncertainty of phase evaluation using Fourier transform method. Speckle noise of the image was not the

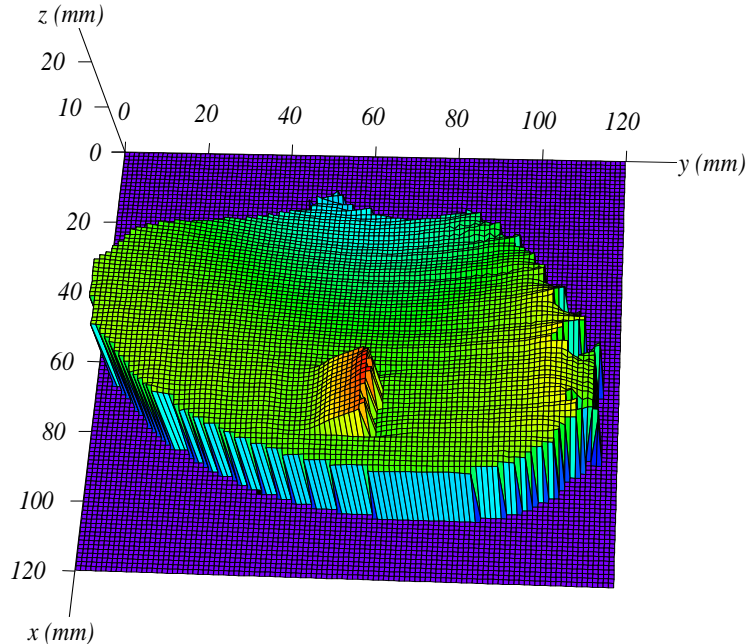


Fig. 10. 3D profile of the testing sample measured from the proposed scheme.

major factor because a white light illumination was employed. Since the frequency of the lower one was designed not sensitive to the depth discontinuities, the spectra of the modulated signal and the DC term might be overlapped in the frequency domain [24]. Thus, more errors could be induced to the low-frequency phases while phase evaluation by Fourier transform method. The compounding errors were harmful to phase unwrapping. Fortunately, by choosing a proper fringe period, it was still permissive for jump correction even though the errors were involved. As shown in Fig. 8(b), the dark areas where bad data were bestrewed on the fan blades were mainly caused by such kind of errors.

Figure 10 shows the 3D shape measured by our proposed method. The experimental result demonstrated that the quality of the measure was very high. There were no noticeable errors on this measurement. This measurement result was also compared with the data obtained from the standard scanning stylus surface profiler. Two measurement results agreed very well (in the micron range accuracy).

7. Conclusion

We have presented a projected fringe profilometry using a two-frequency pattern to achieve micron-range absolute shape measurement for complex objects with depth discontinuities. To suit the needs of high-accuracy measurements, a digital two-frequency pattern has been designed and fabricated based on the optical lithography technique. The designed pattern can substantially increase the measurement accuracy because it offers (1) high geometrical accuracy; (2) high contrast ratio; and (3) very low high-order harmonic distortions.

It requires only one measurement frame to inspect discontinuous surfaces. The experimental result has demonstrated that the quality of the measure is in the micron range accuracy. This makes it possible for a single-shot measurement of dynamic objects with discontinuities.

Acknowledgments

This work was performed under the support of the *Aim for the Top University Plan*. The authors are also grateful for support from the Advanced Crystalline Opto-Electronics Science and Technology Research Center.